A Modified LSR Algorithm Based on the Critical Value of Characteristic Slopes for RAIM

JING ZHAO[1], **DAN SONG**[2], **CHENGDONG XU**[1], **AND XUEEN ZHENG**[1]
[1]Beijing Institute of Technology, Beijing 100086, China
[2]Beihang University, Beijing 100191, China

Corresponding author: Dan Song (songdan0207@163.com)

ABSTRACT Utilizing the least squares residuals (LSR) algorithm to detect the faulty satellite, the faulty satellite with a large characteristic slope will bring a high miss detection risk (MDR) and that with a small characteristic slope will bring a high false alert risk (FAR). However, the magnitude of characteristic slopes whether large or small is currently indefinite. In this paper, analyzing the MDR whether exceeding its allowable value or not, we propose the critical value of characteristic slopes to define the magnitude of a characteristic slope. The slope with the value larger than the critical one can be defined as a large slope whereas the slope with a value smaller than the critical one can be defined as a small slope. To reduce the fault detection risk of the LSR algorithm, including the MDR caused by a large slope faulty satellite and the FAR caused by a small slope faulty satellite, a modified LSR algorithm based on the critical value of characteristic slopes is proposed. In the modified algorithm, the most potential faulty satellite is determined via correlation analysis. Then, a subset fault detection methodology will be used to reduce the MDR when the most potential faulty satellite owns a large slope, whereas a threshold amplification fault detection methodology will be used to reduce the FAR when the most potential faulty satellite owns a small slope. The performance evaluation simulations of the modified LSR algorithm show that both the MDR caused by a large slope faulty satellite and the FAR caused by a small slope faulty satellite could be effectively reduced.

INDEX TERMS GNSS, fault detection, receiver autonomous integrity monitoring (RAIM), least squares residuals (LSR) algorithm, characteristic slope.

I. INTRODUCTION

Integrity is one of the required navigation performances for Global Navigation Satellite System (GNSS) aviation users [1], [2]. Integrity monitoring, which can be provided both at the system level and at the user level, is used to protect users against potentially harmful GNSS navigation malfunctions [3]. The main integrity monitoring approach at the user level is the receiver autonomous integrity monitoring (RAIM). Most RAIM algorithms are designed to detect the faulty satellite based on statistical consistency checks with redundant measurements [4], [5].

The snapshot algorithm is the most widely used RAIM algorithm for its small calculation amount and simple operation. And the least squares residual (LSR) algorithm is one of the classical snapshot RAIM algorithm, which takes the sum of squares for pseudorange residuals as the test statistic to detect satellite fault [6], [7], [28].

The LSR algorithm was initially invalid for multiple faulty satellites, only efficacious for single faulty satellite detection. Many algorithms have been designed to detect multiple faulty satellites [8], [30]. For example, Schroth *et al.* [9] proposed the range consensus (RANCO) algorithm, which can detect multiple faulty satellites through calculating position solution for each four-satellite subset and comparing this estimate with the pseudoranges of all the satellites not contributing to this solution. Yang and Xu [10] used a kind of alternative RAIM algorithm based on robust estimation, which can not only detect multi-failures, but also control the influences of near failure observation. The RANCO algorithm and alternative RAIM algorithm are implement in the multiple faulty domain. A multiple faults detection algorithm was proposed in the position domain also, the multiple hypothesis solution separation (MHSS) algorithm, which detect faults

---

The associate editor coordinating the review of this manuscript and approving it for publication was Masood Ur-Rehman.

via protection level calculation under each fault mode [11]. Blanch *et al.* [8] modified this algorithm to improve the probability of multiple fault satellites detection.

Except invalid detection for multiple faulty satellites, the fault detection probability for minor observation bias using the snapshot LSR algorithm is low. Many researches have been devoted to improve the fault detection probability for minor observation bias through modifying the LSR algorithm. The modification approaches can be classified into three categories. The first is to revise the pseudorange residuals using the accurate receiver clock error, making the test statistic of the LSR algorithm more sensitive to the minor observation bias. For example, Xu and Li [12] established a quadratic function model to predict the receiver error in current epoch and Angrisano *et al.* [13] obtained the accurate receiver clock error from external equipment. The second is to accumulate test statistics for several epochs. For example, Wen-Xiang *et al.* [14] used the accumulated the sum of squares for pseudorange residuals for multiple epochs as the test statistic, and Hai *et al.* [15] further improved the accumulated test statistic by non-coherent processing. The third is to improve the pseudorange residual calculation methodology. Yang *et al.* [16] replaced the usual least squares to total least squares(TLS), improving minor observation bias detection probability through resisting the erroneous perturbation in the transformation and back-substitution of the observation matrix.

All above LSR algorithm modification approaches can significantly improve the fault detection probability for minor observation bias. However, due to the statistical independence between the position error and the pseudorange residual, the observation bias reflected by a small pseudorange residual may bring a large position error and that reflected by a large pseudorange residual may bring a small position error [17]. The magnitude of the pseudorange residual and the position error are decided by a geometric characteristic of the faulty satellite which owns observation bias. Feng *et al.* [18] has defined a geometric characteristic related parameter to qualitatively describe the size relationship of the position error and the pseudorange residual, named as the characteristic slope. The observation bias of a large slope faulty satellite will bring a large position error and a small pseudorange residual, whereas that of a small slope faulty satellite will bring a small position error and a large pseudorange residual.

Because the original intention of RAIM is to alert hazardous misleading information (HMI) [19], the position fault, i.e. the position with error exceeding the alert limit, should be more concerned rather than the satellite fault. If the position fault was caused by a large slope faulty satellite, it would be in a high miss detection risk (MDR) using the LSR algorithm. And if the position fault was caused by a small slope faulty satellite, it would be in a high false alert risk (FAR). The way just by improving the fault detection probability for observation bias would be favorable for reducing the MDR for position fault caused by a large slope faulty satellite, but unfavorable for increasing the FAR for position fault

caused by a small slope faulty satellite. Some researchers are devoted to reduce the fault detection risk, especially the MDR. For example, Madonna *et al.* [20] proposed NIO-RAIM algorithm in which the pseudorange residual for each satellite in the test statistic is weighted to reduce the slope value. Lee [21] proposed the Critically Weighted Average Solution (OWAS) algorithm, also weighted the pseudorange residual. The weights used by Lee are analytically derived in the position domain. Joerger *et al.* [22], [23] designed a Non-Least-Squares (NLS) detector, which can minimize the MDR. Blanch *et al.* [8] present an algorithm that simultaneously allocates the integrity and continuity budget among the failure modes in MHSS to minimize the MDR. These algorithms are all effective on MDR reduction, but show poor performance on FAR reduction.

In this paper, we utilize the property of the critical value of characteristic slopes to modify the LSR algorithm, making the LSR test statistic be more consistent with the position error. At first, we propose a clear boundary, named as the critical slope, to define magnitude of the slopes for each satellite-user geometry. A slope larger than the critical slope defines as the large slope while a slope smaller than the critical slope defines as the small slope. Then we propose a fault detection threshold amplification methodology to reduce the FAR for the small slope faulty satellite and a subset fault detection methodology to reduce the MDR for the large slope faulty satellite. Finally, we propose a modified LSR algorithm based the critical value of characteristic slopes and the two methodologies to reduce the risk of position fault detection.

II. TECHNICAL BACKGROUND
A. THE LSR ALGORITHM FOR RAIM
According to the pseudorange position principle, the linearized observation equation between the receiver and the visible satellites is as follows:

$$Z = HX + \varepsilon \qquad (1)$$

where
Z is the pseudorange vector,
H is the linear observation matrix,
X is the 4×1 state vector and $X = [x, y, z, \Delta t]^T$, with x, y, and z are the three-dimensional positions of the user in the local Cartesian coordinate (ENU),
Δt is the clock error for GNSS.
ε is the observation error vector. Each element in ε represents the observation error for a visible satellite. The observation error of for each visible satellite includes the noise and the bias. The bias is caused by the satellite fault, only existing in the pseudorange of faulty satellite. In this paper, the observation noise is assumed to be independent White Gaussian Noise (WGN) with mean zero and variance σ_0^2.

The least squares solution for X in (1) is

$$\hat{X} = (H^T H)^{-1} H^T Z \qquad (2)$$

The solution error for X, signed as μ, can be expressed as follows:

$$\mu = X - \hat{X} = -(H^T H)^{-1} H^T \varepsilon \tag{3}$$

Setting $A = (H^T H)^{-1} H^T$,

$$\mu = -A\varepsilon \tag{4}$$

The pseudorange residual vector, recorded as ω, is defined by combining (1) and (2) as follows:

$$\begin{aligned} \omega &= Z - \hat{Z} = Z - H\hat{X} \\ &= [I - H(H^T H)^{-1} H^T](HX + \varepsilon) \\ &= [I - H(H^T H)^{-1} H^T]\varepsilon \end{aligned} \tag{5}$$

Setting $S = [I - H(H^T H)^{-1} H^T]$,

$$\omega = S\varepsilon \tag{6}$$

The fault detection using the LSR algorithm is theoretically a binary hypothesis test, with the test statistic Ts constructed using the sum of squares for ω as follows:

$$Ts = \omega^T \omega \Big/ \sigma_0^2 \tag{7}$$

where $\omega^T \omega$ is usually abbreviated as SSE. The satellite fault can be detected using this Ts because it can reflect the observation error.

The Ts obeys the standard χ^2 distribution with freedom degree of K-4 with no faulty satellite, where K represents the number of all-in-view satellites and The detection threshold for Ts, signed as T_D, obeys the α-quantile of standard χ^2 distribution, i.e., $P(X > T_D) = \alpha X \sim \chi^2(K - 4)$.

B. DEFINITION OF MDR AND FAR FOR LSR ALGORITHM

In practical applications, the users are concerned with the position fault rather than the satellite fault because the position fault directly makes the users in danger. Because Ts in (7), constructed in measurement domain [18], cannot visually reflect the position fault, the LSR algorithm would have high fault detection risk. In detail, Although Ts reflects the existence of the observational bias for a faulty satellite, the observational bias may just lead to slightly position error, far from reaching the level of position fault [32].

There are two indicators to detect the fault: miss detection risk (MDR) and false alert risk (FAR). In this paper, MDR and FAR are defined choosing the vertical position error (VPE) as an example. The MDR is the probability of miss detection when the $|VPE|$ exceeds the Vertical Alarm Limit (VAL), whereas the FAR is the probability of false alert when the $|VPE|$ does not exceed VAL.

Setting Event C as "$Ts \geq T_D$", and Event D as "$|VPE| \geq VAL$", MDR can be expressed as $P(\bar{C}D)$ and FAR can be expressed as $P(C\bar{D})$. Here we divide $P(\bar{C}D)$ and $P(C\bar{D})$ into three parts according to the number of faulty satellites [19], [24].

$$P(\bar{C}D) = P(\bar{C}D, 0F) + P(\bar{C}D, 1F) + P(\bar{C}D, \geq 2F) \tag{8}$$

$$P(C\bar{D}) = P(C\bar{D}, 0F) + P(C\bar{D}, 1F) + P(C\bar{D}, \geq 2F) \tag{9}$$

where

0F represents there exists no faulty satellite,

1F represents there exists only one faulty satellite,

$\geq 2F$ represents there exists two or more faulty satellites.

According to the conditional probability formula,

$$P(\bullet, iF) = P(\bullet \,|iF\,)P(iF) \tag{10}$$

where $\bullet$ represents $\bar{C}D$ or $C\bar{D}$, and $i = 0, 1, \geq 2$.

$$P(0F) = (1 - P_{sat})^K \tag{11}$$

$$P(1F) = C_K^1 P_{sat}(1 - P_{sat})^{K-1} \tag{12}$$

$$P(\geq 2F) = P_{total} + \sum_{n=2}^{K} C_K^n (P_{sat})^n (1 - P_{sat})^{K-n} \tag{13}$$

where P_{sat} is the prior probability of satellite fault. $P(\geq 2F)$ are composed of two parts, respectively the prior probability of multiple satellite fault caused by the same reason and independent reasons. P_{sat} is set as 1.0×10^{-5} and P_{total} is set as 1.3×10^{-8} in [24].

Because the random parts of μ and ω are independent [24], [25],

$$P(\bar{C}D \,|0F\,) = P(\bar{C} \,|0F\,) \cdot P(D \,|0F\,) \tag{14}$$

$$P(\bar{C}D \,|1F\,) = P(\bar{C} \,|1F\,) \cdot P(D \,|1F\,) \tag{15}$$

$$P(C\bar{D} \,|0F\,) = P(C \,|0F\,) \cdot P(\bar{D} \,|0F\,) \tag{16}$$

$$P(C\bar{D} \,|1F\,) = P(C \,|1F\,) \cdot P(\bar{D} \,|1F\,) \tag{17}$$

$P(\bar{C}D|0F)$ and $P(C\bar{D}|0F)$ can be calculated according to the distributions of VPE and Ts. According to (4), the VPE, which is the third component of μ, obeys the distribution:

$$VPE \sim N(0, a_v^2 \sigma_0^2) \tag{18}$$

where

$N(\mu, \sigma^2)$ represents a normal distribution with mean μ and variance σ^2,

a_v^2 is the sum of squares for all elements in Row 3 of A and $a_v^2 = \sum_{i=1}^{K} a_{3i}^2$. Actually, a_v is the vertical dilution of precision (VDOP), which is proved in Appendix A.

Then, $P(D|0F)$ and $P(\bar{D}|0F)$ can be calculated as follows:

$$P(D|0F) = 1 - P(|VPE| \leq VAL) = 1 - \int_{-VAL}^{VAL} g_0(x)dx \tag{19}$$

$$P(\bar{D}|0F) = P(|VPE| \leq VAL) = \int_{-VAL}^{VAL} g_0(x)dx \tag{20}$$

where $g_0(x)$ is the probability density function (PDF) of the VPE with no faulty satellite, and

$$g_0(x) = \frac{1}{\sqrt{2\pi a_v^2 \sigma_0^2}} \exp\left(-\frac{(x)^2}{2a_v^2 \sigma_0^2}\right) \tag{21}$$

According to (6) and (7), Ts obeys the distribution:

$$Ts \sim \chi^2(K - 4) \tag{22}$$

where $\chi^2(v)$ represents standard χ^2 distribution with the freedom degree of v, K is the number of visible satellites

in view. Then, $P(C|0F)$ and $P(\bar{C}|0F)$ can be calculated as follows:

$$P(C|0F) = P(Ts \geq T_D) = \alpha \tag{23}$$

$$P(\bar{C}|0F) = 1 - P(Ts \geq T_D) = 1 - \alpha \tag{24}$$

where α is the quantile for chosen T_D.

Finally, $P(\bar{C}D|0F)$ and $P(C\bar{D}|0F)$ can be respectively calculated as:

$$\begin{aligned}
P(\bar{C}D|0F) &= P(\bar{C}|0F)P(D|0F) \\
&= (1-\alpha) \cdot (1 - \int_{-VAL}^{VAL} g_0(x)dx) \\
&= (1-\alpha)(1 - \int_{-VAL}^{VAL} \frac{1}{\sqrt{2\pi a_v^2 \sigma_0^2}} \exp\left(-\frac{(x)^2}{2a_v^2\sigma_0^2}\right) dx)
\end{aligned} \tag{25}$$

$$\begin{aligned}
P(C\bar{D}|0F) &= P(C|0F)P(\bar{D}|0F) \\
&= \alpha \int_{-VAL}^{VAL} g_0(x)dx \\
&= \alpha \cdot \left(\int_{-VAL}^{VAL} \frac{1}{\sqrt{2\pi a_v^2 \sigma_0^2}} \exp\left(-\frac{(x)^2}{2a_v^2\sigma_0^2}\right) dx\right)
\end{aligned} \tag{26}$$

Analyzing (25) and (26), we observed that a large a_v would lead to a large $P(\bar{C}D|0F)$ and a small $P(C\bar{D}|0F)$ with fixed the VAL and σ_0 values.

$P(\bar{C}D|1F)$ and $P(C\bar{D}|1F)$ can be also calculated according to the distributions of VPE and Ts. According to (4), the VPE obeys the distribution

$$VPE \sim N(-a_{3m}\xi_b, a_v^2\sigma_0^2) \tag{27}$$

where

m represents the number of the m-th visible faulty satellite, notated as VS_m,

a_{3m} is the element in Row 3 and Column m of $\boldsymbol{A}$

ξ_b is the observation bias of the faulty satellite.

Then, $P(D|1F)$ and $P(\bar{D}|1F)$ can be calculated as follows:

$$P(D|1F) = 1 - P(|VPE| \leq VAL) = 1 - \int_{-VAL}^{VAL} g(x)dx \tag{28}$$

$$P(\bar{D}|1F) = P(|VPE| \leq VAL) = \int_{-VAL}^{VAL} g(x)dx \tag{29}$$

where $g(x)$ is the probability density function (PDF) of the VPE with faulty satellite VS_m, and

$$g(x) = \frac{1}{\sqrt{2\pi a_v^2 \sigma_0^2}} \exp\left(-\frac{(x + a_{3m}\xi_b)^2}{2a_v^2\sigma_0^2}\right) \tag{30}$$

Ts obeys the distribution:

$$Ts \sim \chi^2(K - 4, \lambda) \tag{31}$$

where $\chi^2(v, \lambda)$ represents non-central χ^2 distribution with the freedom degree of v and the decentralized parameter of λ.

The λ value can be seen in (32), which is specifically deduced in [26]:

$$\lambda = \left(\frac{\xi_b}{\sigma_0}\right)^2 s_{mm} \tag{32}$$

Then, $P(C|1F)$ and $P(\bar{C}|1F)$ can be calculated as follows:

$$P(C|1F) = P(Ts \geq T_D) = \int_{T_D}^{+\infty} f(x)dx \tag{33}$$

$$P(\bar{C}|1F) = 1 - P(Ts \geq T_D) = \int_0^{T_D} f(x)dx \tag{34}$$

where $f(x)$ is the probability density function (PDF) of Ts, and

$$f(x) = \frac{1}{2}e^{-(x+\lambda)/2}\left(\frac{x}{\lambda}\right)^{v/4-1/2}I_{v/2-1}(\sqrt{\lambda x}) \tag{35}$$

where $I_r(y) = (y/2)^r \sum_{j=0}^{\infty} \frac{(y^2/4)^j}{j!\Gamma(v+j+1)}$ is the Bessel functions of the first kind.

Finally, $P(\bar{C}D|1F)$ and $P(C\bar{D}|1F)$ can be respectively calculated as:

$$\begin{aligned}
&P(\bar{C}D|1F) \\
&= P(\bar{C}|1F)P(D|1F) \\
&= \int_0^{T_D} f(x_1)dx_1 \cdot (1 - \int_{-VAL}^{VAL} g(x_2)dx_2) \\
&= \left(\int_0^{T_D} \frac{1}{2}e^{-(x_1+\lambda)/2}\left(\frac{x_1}{\lambda}\right)^{v/4-1/2}I_{v/2-1}(\sqrt{\lambda x_1})dx_1\right) \\
&\quad \cdot \left(1 - \int_{-VAL}^{VAL} \frac{1}{\sqrt{2\pi a_v^2\sigma_0^2}} \exp\left(-\frac{(x_2 + a_{3m}\xi_b)^2}{2a_v^2\sigma_0^2}\right) dx_2\right)
\end{aligned} \tag{36}$$

$$\begin{aligned}
&P(C\bar{D}|1F) \\
&= P(C|1F)P(\bar{D}|1F) \\
&= \int_{T_D}^{+\infty} f(x_1)dx_1 \cdot \int_{-VAL}^{VAL} g(x_2)dx_2 \\
&= \left(\int_{T_D}^{+\infty} \frac{1}{2}e^{-(x_1+\lambda)/2}\left(\frac{x_1}{\lambda}\right)^{v/4-1/2}I_{v/2-1}(\sqrt{\lambda x_1})dx_1\right) \\
&\quad \cdot \left(\int_{-VAL}^{VAL} \frac{1}{\sqrt{2\pi a_v^2\sigma_0^2}} \exp\left(-\frac{(x_2 + a_{3m}\xi_b)^2}{2a_v^2\sigma_0^2}\right) dx_2\right)
\end{aligned} \tag{37}$$

where x_1 represents the Ts and x_2 represents the VPE.

Analyzing (28)-(30) and (33)-(35), we concluded that a large $|a_{3m}|$ brings a large $P(D|1F)$ and a small $P(\bar{D}|1F)$ with the fixed VAL, ξ_b, σ_0 and a_v values and a large s_{mm} brings a large $P(C|1F)$ and a small $P(\bar{C}|1F)$ with the fixed T_D, ξ_b and σ_0 values.

Because $P(\bar{C}D| \geq 2F)$ and $P(C\bar{D}| \geq 2F)$ are more complicated and the LSR algorithm is invalid for multiple faulty satellites detection, here we no longer give the calculation expression for $P(\bar{C}D| \geq 2F)$ and $P(C\bar{D}| \geq 2F)$.

C. DEFINITIONS OF MAXIMUM ALLOWABLE VALUE FOR $P(\bar{C}D|1F)$

In RAIM, both miss detection and false alert need to be avoided because miss detection leads to hazardous misleading information (HMI) and false alert leads to observation resource waste [27]. Specifically, miss detection is more noticed because its resulting HMI may bring immeasurable losses to users. Therefore, the maximum allowable MDR should be limited to fully protect the safety of users, which is named as MDR requirement and signed as MDR_{req}.

Detecting position fault with LSR algorithm, MDR should be less than MDR_{req} for protecting the user away from HMI, which can be expressed as:

$$\begin{pmatrix} P(\bar{C}D|0F)P(0F) + P(\bar{C}D|1F)P(1F) \\ + P(\bar{C}D| \geq 2F)P(\geq 2F) \end{pmatrix} \leq MDR_{req} \quad (38)$$

The maximum allowable value for $P(\bar{C}D|1F)$, notated as $[P(\bar{C}D|1F)]_a$, can be derived as follows:

$$[P(\bar{C}D|1F)]_a = \frac{\begin{pmatrix} MDR_{req} - P(\bar{C}D|0F)P(0F) \\ -P(\bar{C}D| \geq 2F)P(\geq 2F) \end{pmatrix}}{P(1F)} \quad (39)$$

where $P(\bar{C}D| \geq 2F)$ could be set as a maximum value $P(\bar{C}D| \geq 2F) = 1$, because LSR algorithm is invalid for multiple satellites fault detection.

Substitute (11)-(13) and (25) into (39),

$[P(\bar{C}D|1F)]_a$

$$= \frac{\begin{pmatrix} MDR_{req} - (1-\alpha) \cdot (1 - \int_{-VAL}^{VAL} g_0(x)dx)(1-P_{sat})^K \\ -(P_{total} + \sum_{n=2}^{K} C_K^n (P_{sat})^n (1-P_{sat})^{K-n}) \end{pmatrix}}{C_K^1 P_{sat}(1 - P_{sat})^{K-1}} \quad (40)$$

then we can observe that $[P(\bar{C}D|1F)]_a$ is decided by a_v and K with the fixed MDR_{req}, σ_0, α, P_{sat} and P_{total} values, i.e. $[P(\bar{C}D|1F)]_a$ value is related to the geometry.

Fig.1 shows $[P(\bar{C}D|1F)]_a$ with different a_v^2 for 8, 9, and 10 all-in-view satellites for LSR algorithm, under the condition of $MDR_{req} = 2.0 \times 10^{-7}$, $\sigma_0 = 4m$, $\alpha = 1.0 \times 10^{-6}$, $P_{sat} = 1.0 \times 10^{-5}$, and $P_{total} = 1.3 \times 10^{-8}$. $[P(\bar{C}D|1F)]_a$ keeps constant with a_v^2 less than 4 because $P(\bar{C}D|0F)$ is almost 0. With a_v^2 larger than 4, $P(\bar{C}D|0F)$ significantly increased. Thus $[P(\bar{C}D|1F)]_a$ decreases with a_v^2 addition. This figure illustrates that LSR algorithm cannot be used to detect satellite fault with a_v^2 larger than about 5.8 for 8, 9, and 10 all-in-view satellites because $[P(\bar{C}D|1F)]_a < 0$, which means no matter how low $P(\bar{C}D|1F)$ is, $P(\bar{C}D)$ will be larger than MDR_{req}. Moreover, $[P(\bar{C}D|1F)]_a$ decreases with all-in-view satellites addition at a fixed a_v^2 value.

In the following, the MDR and the FAR mentioned below means the MDR and the FAR with a single faulty satellite $P(D)$, $P(\bar{D})$, $P(C)$, $P(\bar{C})$, $P(\bar{C}D)$ and $[P(\bar{C}D)]_a$ respectively refer to $P(D|1F)$, $P(\bar{D}|1F)$, $P(C|1F)$, $P(\bar{C}|1F)$, $P(\bar{C}D|1F)$ and $[P(\bar{C}D|1F)]_a$.
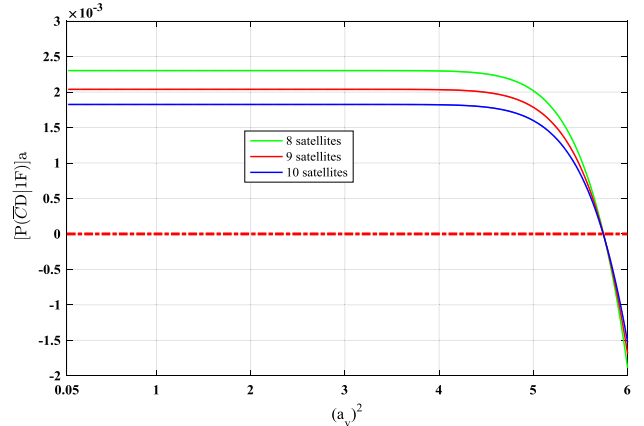

FIGURE 1. $[P(\bar{C}D|1F)]_a$ for the LSR algorithm.

D. THE CHARACTERISTIC SLOPE AND RELATIONSHIP BETWEEN MDR/FAR AND SLOPE

Although the position error and the test statistic are independent, the quantity relationship between VPE and Ts can be described with a geometry-related parameter, the characteristic slope. Feng et al. [18] defined the horizontal and vertical characteristic slopes for each visible satellite according to the parameters in the matrix A and the matrix S. Because A and S are both only related with the observation matrix H, which characterizes the geometry between the users and all-in-view satellites, the characteristic slopes for each visible satellite are geometric characteristic parameters. In this paper, we only discuss the VPE and the vertical characteristic slope. Besides the vertical characteristic slope is abbreviated as the slope in the following.

The slope for VS_i, notated as $Slope_i$, is defined with the related elements in the matrix A and S as follows:

$$Slope_i = \sqrt{\frac{a_{3i}^2}{s_{ii}}} \quad (41)$$

where a_{3i} is the element in Row 3 and Column i of A in (4), s_{ii} is the $i - th$ diagonal element of S in (6).

Analyzing (41), a large $Slope_i$ value may be caused by a large a_{3i} and a small s_{ii} while a small $Slope_i$ value may be caused by a small a_{3i} and a large s_{ii}. According to (27) and (31), a_{3m} and s_{mm} respectively characterize the VPE and Ts, both caused by the observation bias for the faulty satellite VS_m. Therefore, the observation bias of large slope faulty satellite will bring large VPE and small SSE while that of small slope faulty satellite will bring small VPE and large SSE.

Here use a concrete example with conditions shown in Tab.1 to visually analyze the relationship between the MDR (FAR) and the slope for different visible satellites.

Tab.2 records a_{3m}, s_{mm}, and $Slope_m$ values for each visible satellite in this example. PRN 23 and PRN 30 respectively have the maximum and minimum slope values.

The distributions of VPE and Ts for PRN 23 and PRN 30 with 0m and 40m(10 σ_0) observation bias ξ_b are presented

TABLE 1. Conditions of example.

Parameter	Value
Constellation	GPS
Masking angle	10°
σ_0	4 m
VAL	50 m
IR_{req}	2×10^{-7}
T_D	35.888 ($\alpha = 10^{-6}$)
Receiver position	north latitude 65°, east longitude 145°, height 0 m
Simulation epoch	2018-12-6 12:25:00

TABLE 2. a_{3m}, s_m and $VSlope_m$ for VS_m (m = 1,…,K).

Parameter	PRN				
	2	10	13	19	21
a_{3m}	0.169	-0.621	0.344	0.653	-0.268
s_{mm}	0.421	0.492	0.659	0.598	0.557
$VSlope_m$	0.261	0.886	0.424	0.845	0.359

Parameter	PRN			
	23	29	30	31
a_{3m}	-0.981	-0.373	0.126	0.951
s_{mm}	0.375	0.650	0.726	0.522
$VSlope_m$	1.603	0.463	0.148	1.316

in Fig.2. In Fig.2 (a) and Fig.2 (b), the red dotted lines represent the VAL and the shadow area represents the probability of the VPE exceeding the VAL. Because of the large $|a_{3m}|$ value ($a_{3m} = -0.981$) of PRN 23, the PDF curve of VPE with $\xi_b = 40m$ apparently moves to the left of that with $\xi_b = 0m$. Therefore, VPE may exceeds VAL with $\xi_b = 40m$ for PRN23. The shadow area represents the probability of the VPE exceeding the VAL, i.e., $P(D)$. On the contrary, because of the small $|a_{3m}|$ value ($a_{3m} = 0.126$) of PRN 30, the PDF curve for VPE with $\xi_b = 40m$ slightly moves to the right of that for VPE with $\xi_b = 0m$, and the probability of the VPE exceeding the VAL to PRN10 is almost 0.

In Fig.2 (c) and Fig.2 (d), the red dotted lines represent the T_D and the shadow area represents the probability of the Ts exceeding the T_D. Both of the PDF curves of Ts with $\xi_b = 40m$ for PRN 23 and PRN30 apparently moves to the right of these with $\xi_b = 0$. However, the probability of Ts exceeding T_D for PRN 23 is lower than that for PRN 30, because of the s_{mm} value for PRN 23 (0.375), is smaller than that for PRN 30 (0.726).

Tab.3 records the $P(D)$, $P(\bar{D})$, $P(C)$, $P(\bar{C})$, $P(\bar{C}D)$, and $P(C\bar{D})$ for PRN 23 and PRN 30 with $\xi_b = 40m$.

$P(\bar{C}D)$ of PRN23, owning the large slope, is larger than $[P(\bar{C}D)]_a = 0.002$, which is calculated according to (40)
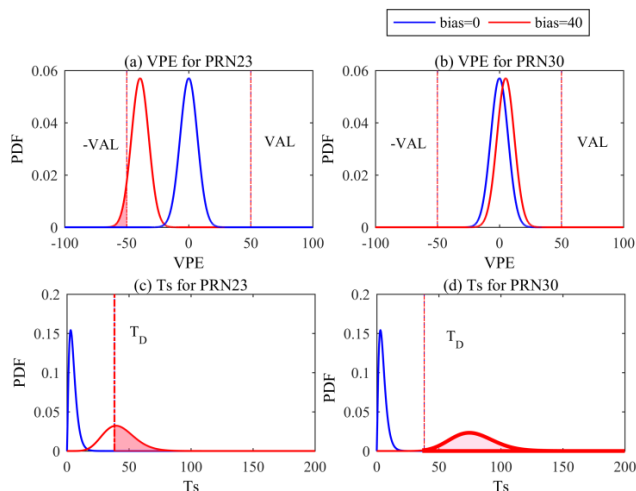

FIGURE 2. Distributions of *VPE* and *Ts* for PRN 23 and PRN 30 with 40m observation bias.

with parameters in Tab.1. We observe that the users would be dangerous because MDR exceeds its max allowable value. Meanwhile, $P(C\bar{D})$ of PRN 30 is 0.998, meaning that PRN 30 would have 99.8% probability of false alert if there was 40 m bias in its pseudorange.

According to Fig.2. and Tab.3, we concluded that a large slope faulty satellite should have a high MDR while a small slope faulty satellite should have a high FAR.

TABLE 3. MDR and FAR for PRN2 and PRN10.

PRN	$P(D)$	$P(\bar{D})$	$P(C)$	$P(\bar{C})$	$P(\bar{C}D)$	$P(C\bar{D})$
23	0.062	0.938	0.678	0.322	0.020	0.636
30	6.23e-11	1.000	0.998	0.002	0.000	0.998

III. DERIVATION OF THE OPTIMAL SLOPE

In this section, we propose the critical slope for satellite-user geometry, signed as $Slope_{cri}$ and derived from the analysis of MDR whether exceeding its allowable value or not, to define the magnitude of the slopes. Then, the slope larger than $Slope_{cri}$ can be taken as a large slope whereas the slope smaller than $Slope_{cri}$ can be taken as a small slope. We still use the example with conditions shown in Tab.1 to concisely show the derivation process.

Fig.3 presents $\lg P(\bar{C}D)$ and $\lg P(C\bar{D})$ values with observation bias from 1 m to 1000m for 4 different satellites, PRN13, PRN19, PRN23 and PRN31. The $\lg[P(\bar{C}D)]_a$ value is marked with a green dotted line in the left panel of Fig.3, $[P(\bar{C}D)]_a = 0.002$ in this example. The orders of the $\lg P(\bar{C}D)$ and $\lg P(C\bar{D})$ curves visually illustrate that $P(\bar{C}D)$ increases with the slope value addition while $P(C\bar{D})$ decreases with the slope value addition.

As shown in Fig.3, $P(\bar{C}D)$ is larger than $[P(\bar{C}D)]_a$ with observation bias from about 30m to 60m for PRN23. It would
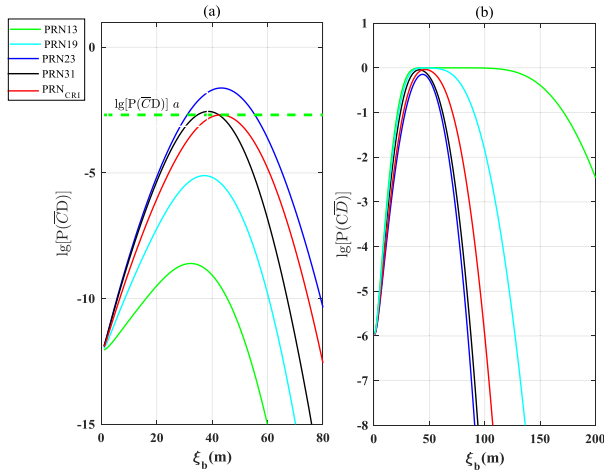
FIGURE 3. $P(\bar{C}D)$ and $P(C\bar{D})$ for 4 different faulty satellites.

be unfortunate and dangerous for the user to utilize the LSR algorithm to detect fault of PRN23 because the MDR exceeds its allowable value with some specific observation bias values. The $\lg P(\bar{C}D)$ curve for PRN31 is nearly tangent to the $\lg[P(\bar{C}D)]_a$ curve. And the $\lg P(\bar{C}D)$ curves for PRN13, and PRN19 are always lower than the $\lg[P(\bar{C}D)]_a$ value, meaning it would be safe for the user to detect fault with PRN13 and PRN19 and no matter how large the observation bias is. However, the $\lg P(\bar{C}D)$ curves of PRN13 and PRN19 are far from the $\lg[P(\bar{C}D)]_a$ curve, which means LSR algorithm is too safe for PRN13 and PRN19, leading to high FAR. As seen in Fig.3, both $\lg P(C\bar{D})$ curves of PRN13 and PRN29 have a segment keeping zero, i.e., $P(C\bar{D}) = 1$. Especially for PRN13, $P(C\bar{D})$ maintains 100% with observation bias from about 60m to 120m.

The shape of $\lg P(\bar{C}D)$ and $\lg P(C\bar{D})$ curves are decided by the slope value with a fixed geometry. Analyzing the MDR and the FAR for 4 satellites in Fig.3, the best fault detection performance of LSR algorithm is to PRN31, for which $\lg P(\bar{C}D)$ curve is nearly tangent to the $\lg[P(\bar{C}D)]_a$ curve and almost not have the segment of $P(C\bar{D}) = 1$. Let us speculated that there exists a slope which makes the $\lg P(\bar{C}D)$ curve just tangent to the $\lg[P(\bar{C}D)]_a$ curve. It will be the critical one among all slope values, minimizing the FAR with the premise of the MDR not exceeding its allowable value. Then the slope larger than the critical one will lead to the MDR exceeding its allowable value with some specific observation bias values. The slope smaller than the critical one could satisfy the MDR not exceeding its allowable value but it will increase the FAR.

According to (36), the critical slope, is the solution of the following equation:

$$\max\left[\int_0^{T_D} f(x_1)dx_1 \bullet (1 - \int_{-VAL}^{VAL} g(x_2)dx_2)\right] = [P(\bar{C}D)]_a$$

(42)

where $f(x_1)$ and $g(x_2)$ should be taken as a function of ξ_b. The parameter s_{mm} in λ of $g(x_2)$ should be replaced by $(a_{3m}/Slope_{cri})^2$ according to (41), where $Slope_{cri}$ is the notation of the critical slope.

The analytical solution of $Slope_{cri}$ should be calculated with two steps. The first is to find a ξ_b value which satisfies $d(P(\bar{C}D))/d\xi_b = 0$, signed as $[\xi_b]_{max}$. $[\xi_b]_{max}$ will be a function of $Slope_{cri}$. The second is to solve the equation of $[P(\bar{C}D)]_{|\xi_b=[\xi_b]_{max}} = [P(\bar{C}D)]_a$. Because $f(x_1)$ is very complicated, it is hard to solve the equation $d(P(\bar{C}D))/d\xi_b = 0$. Therefore, we cannot find the analytical solution of $Slope_{cri}$.

Though it is hard to get the analytical solution of $Slope_{cri}$, the approximate $Slope_{cri}$ can be obtained by numerical solution process seen in Fig.4, with the fixed VAL, T_D, a_v, σ_0, and a_{3m} values. The initial value of $Slope_{cri}$ is set as $Slope_{med}$, which is the median of slopes for all-in-view satellites. The numerical solution starts from the sub-process of counting l, calculating $h(\xi_b) = [P(\bar{C}D)]_a - \varphi(\xi_b)$ with the ξ_b step of 1m at $Slope_{cri} = Slope_{med}$ and counting the points satisfying $h(\xi_b) < 0$. Here $\varphi(\xi_b)$ represents $P(\bar{C}D)$ in (36) with $\lambda = (a_{3m}/Slope_{cri})^2$. The sub-process should not be terminated until $h(\xi_b) < h(\xi_b - 1)$, which means the function $h(\xi_b)$ reaches the reduction phase. The initial $Slope_{cri}$ is proved to be larger than the real $Slope_{cri}$ with $l > 0$. Thereby $Slope_{cri}$ should be reduced with step of 0.001 until $l = 0$. On the contrary, the initial $Slope_{cri}$ is proved to be smaller than the real $Slope_{cri}$ with $l = 0$. Thereby $Slope_{cri}$ should be increased with step of 0.001 until $l > 0$ and the output $Slope_{cri}$ value should be $Slope_{cri} - 0.001$.

Taking example with conditions of Tab.1, T_D, a_v, and σ_0 are fixed except for a_{3m} because each visible satellite has its own a_{3m} value. We calculated $Slope_{cri}$ using each a_{3m} values recorded in Tab.2, and found that $Slope_{cri}$ keeps constant. Thus it can be deduced that $Slope_{cri}$ is only decided by VAL, T_D, a_v, and σ_0. Once VAL, T_D and σ_0 are fixed, $Slope_{cri}$ has one-to-one correspondence a_v.

Fig.5 presents the relationship between $Slope_{cri}$ and a_v^2 with different numbers of all-in-view satellites under the conditions of $VAL = 50m$ and $\sigma_0 = 4m$. The $Slope_{cri}$-a_v^2 curves are almost straight in the middle section and $Slope_{cri}$ decreases with a_v^2 addition for a fixed number of all-in-view satellites, which illustrates the number of high FAR satellites will be large in the geometry with small VDOP while the number of high MDR satellites will be large in the geometry with large VDOP. Safety to the first, the poor geometry with large VDOP is not conducive to fault detection, because it would lead to most visible satellites in high MDR. Moreover, $Slope_{cri}$ decreases with the number of all-in-view satellites addition at a fixed a_v^2 value. The $Slope_{cri}$-a_v^2 curve is interrupted when the value of a_v^2 reaches about 5.8 because LSR cannot be used to detect satellite for a_v^2 larger than 5.8, which has been proved in Fig.1.

Calculating under the condition of Tab.1, $a_v^2 = 3.053$ and $Slope_{cri} = 1.282$. The $\lg P(\bar{C}D)$ and $\lg P(C\bar{D})$ curves with $Slope_{cri}$ is shown with red color in Fig.3. As seen in
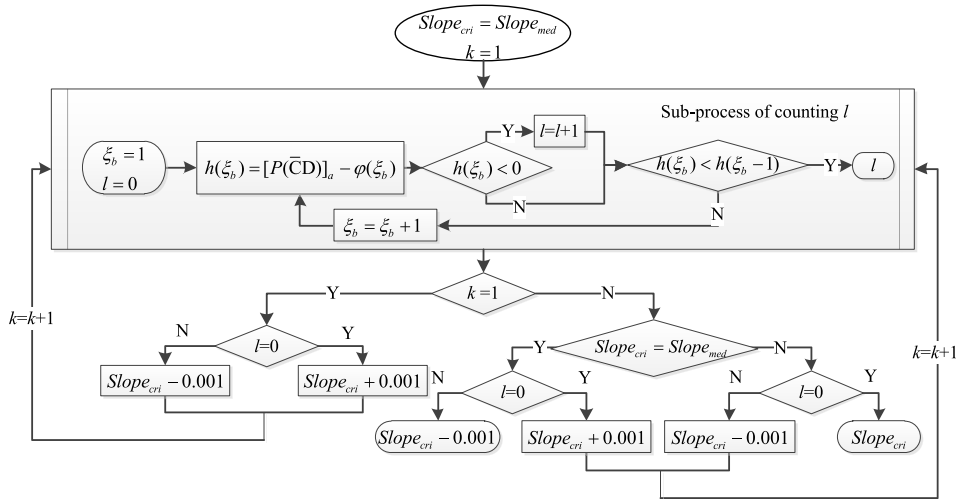
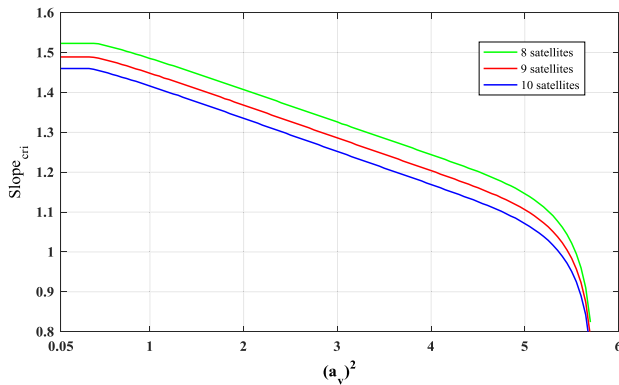**FIGURE 4.** Numerical solution process of $Slope_{cri}$.

FIGURE 5. $Slope_{cri}$ and a_v^2.

Tab.2 And Fig.3, the slopes of PRN23 is obviously larger than $Slope_{cri}$. The MDR of PRN23 exceeds its allowable value significantly. Moreover, the smaller the slope than the $Slope_{cri}$ is, the longer the interval of FAR keeping 100% will be.

Once the $Slope_{cri}$ under a fixed geometry has been computed, the slope larger than the $Slope_{cri}$ can be taken as a large slope whereas the slope smaller than the $Slope_{cri}$ can be taken as a small slope. Utilizing the LSR algorithm to detect a faulty satellite, a large slope faulty satellite will bring high MDR, exceeding its allowable value with observation bias at a certain interval, and a small slope faulty satellite will bring high FAR, may reach 100% with observation bias at a certain interval.

IV. METHODOLOGIES FOR MDR AND FAR REDUCTION

As mentioned above, the visible satellites can be divided into the large slope satellites, for which should reduce the MDR, and the small slope satellites, for which should reduce the FAR. In this section, we propose two methodologies to respectively reduce the risk in two situations.

A. A METHODOLOGY OF FAR REDUCTION FOR A SMALL SLOPE FAULTY SATELLITE

Because $P(\bar{D})$ in (16) cannot be artificially altered for objective existence of the VPE, the only way to reduce FAR caused by a small slope faulty satellite is trying to obtain lower $P(C)$. The test statistic of LSR algorithm is designed as SSE / σ_0^2 because it obeys standard χ^2 distribution when there exists no faulty satellite. Thus, the test threshold can be set according to standard χ^2 distribution.

Here we propose a methodology which amplify the fault detection threshold and still keep SSE / σ_0^2 as the test statistic to reduce $P(C)$ for a small slope faulty satellite. The amplification should under the premise of MDR not exceeding its allowable value. According to (36), the amplification factor of the fault detection threshold, notated as α, is the solution of the following equation

$$\max[\int_0^{\alpha T_D} f(x_1)dx_1 \bullet (1 - \int_{-VAL}^{VAL} g(x_2)dx_2)] = [P(\bar{C}D)]_a \tag{43}$$

similar to (42), it is hard to get the analytical solution of (43). Therefore, α can be numerical solved with the process in Fig.6 and the sub-process of counting l can refer to Fig.4.

Fig.7 presents the relationship between α and $Slope/Slope_{cri}$ for different a_v values when 9 all-in-view satellites with $T_D = 35.888(\alpha = 10^{-6})$, $HAL = 50m$, and $\sigma_0 = 4m$.

α decreases with $Slope/Slope_{cri}$ addition at a fixed a_v and increases with a_v reduction at a fixed $Slope/Slope_{cri}$ value. The α-$Slope/Slope_{cri}$ curve is only determined by a_v with the fixed T_D, HAL and σ_0. It can be fitted as an exponential function

$$\alpha(x) = a(x^b - 1) + 1 \tag{44}$$

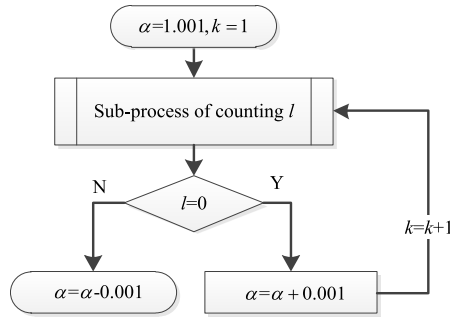where x presents the value of $Slope/Slope_{cri}$. Each a_v corresponds to the fixed a and b values.
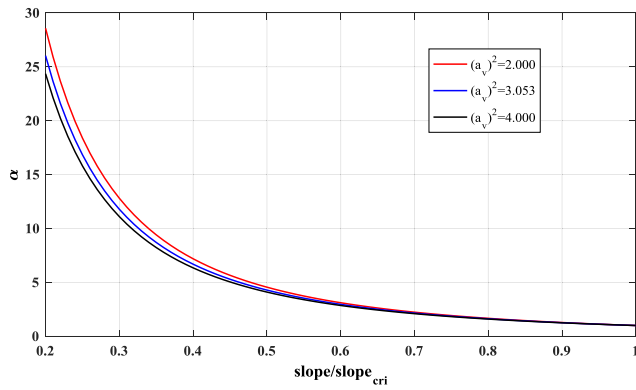
FIGURE 6. Numerical solution process of α.

FIGURE 7. Relationship between α and $Slope/Slope_{cri}$.

FIGURE 8. Fitted α values for $a_v^2 = 3.053$ and K = 9.

FIGURE 9. MDR and FAR with αT_D and T_D.

TABLE 4. a and b values for different a_v^2 and K.

a_v^2	2		3.053		4	
K	K=9	K=10	K=9	K=10	K=9	K=10
a	1.237	1.205	1.159	1.135	1.112	1.095
b	-1.956	-1.955	-1.937	1.932	-1.920	-1.910

Tab. 4 records the fitted values of a and b for different a_v^2 and K. a is positive, decreasing with a_v^2 and K addition. b is negative, and $|b|$ decreases with a_v^2 and K addition.

Fig.8 presents the fitted and the calculated $\alpha - Slope/Slope_{cri}$ curves for $a_v^2 = 3.053$ and K = 9. The fitted $\alpha - Slope/Slope_{cri}$ curve is almost coincides with the calculated curve. The curve fitting indices are $SSE = 0.00233$, $R - Square = 1$, and $RMSE = 0.00532$ respectively, which proves the function of $\alpha(x) = 1.159(x^{-1.937} - 1) + 1$ has a very good fit for the $\alpha - Slope/Slope_{cri}$ curve.

Calculating with the process in Fig.6 under the condition of Tab.1, α value for PRN13 is 9.716. Then, Fig.9 presents the MDR and the FAR for PRN13 with fault detection thresholds of αT_D and T_D. As seen in Fig.9 (a), the $\lg P(\bar{C}D)$ curve for αT_D is higher than that for T_D, but tangent to the $\lg[P(\bar{C}D)]_a$, which means MDR for PRN13 is just not exceeding its allowable value for all observation bias values with fault detection thresholds of αT_D. In Fig.9 (b), the $\lg P(C\bar{D})$ curve for αT_D is
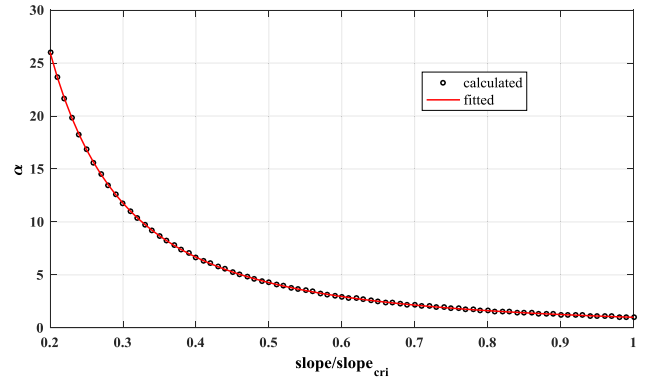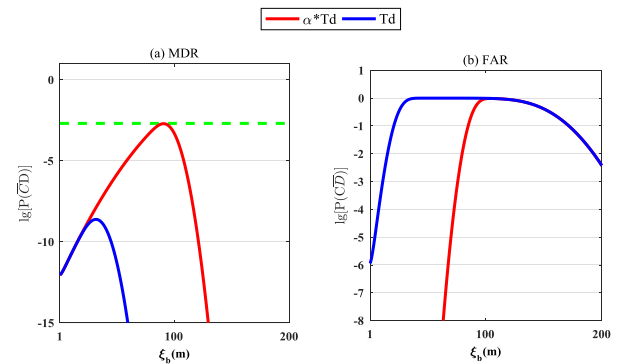
lower than that for T_D with observation bias less than about 100m, which means FAR for PRN13 is reduced with fault detection threshold amplified from T_D to αT_D. Especially, the FAR decreases in magnitude with observation bias less than about 80m.

B. A METHODOLOGY OF MDR REDUCTION FOR A LARGE SLOPE FAULTY SATELLITE

Similar to the first situation, the only way to reduce the MDR caused by a large slope faulty satellite is to reduce the $P(\bar{C})$. However, it is not feasible to reduce $P(\bar{C})$ by only diminishing the fault detection threshold of LSR algorithm, because it would increase the probability of false alert for the no faulty satellite. Here we propose a subset fault detection methodology to reduce $P(\bar{C})$ for a large slope faulty satellite.

We set each 6-satellites as a subset for all-in-view satellites and calculate SSE/σ_0^2 values for each subset. As seen in (32), (34), and (35), the $P(\bar{C})$ is decided by the s_{mm} value. Each 6-satellites subset has its own geometry and the s_{mm} value for the faulty satellite in each subset is different. The satellite which owns small s_{mm} value among all-in-view satellites may own large s_{mm} value among the 6-satellites in a subset. The test statistic to detect the large slope faulty satellite is the SSE/σ_0^2 value of the subset in which the s_{mm} value for the faulty satellite is the maximum among all 6-satellites

subsets. And the fault detection threshold T_D should satisfies $P(X > T_D) = \alpha, X \sim \chi^2(2)$.

Tab.5 records the s_{mm} value of each satellite in the chosen subset for detecting fault on PRN23. The s_{mm} value of PRN23 is 0.367, ranked third in the subset geometry, while the s_{mm} value of PRN23 in Tab.2 is the minimum among all-in-view satellites.

TABLE 5. s_{mm} values for the chosen subset.

PRN	2	10	23	29	30	31
s_{mm}	0.117	0.043	0.367	0.587	0.627	0.259

The fault detection performance to PRN23 and PRN 30 using the chosen subset fault detection mythology is respectively presented in Fig. 10 and Fig.11. Fig. 10 (a) shows the $P(C)$ difference between utilizing the chosen subset and the complete set to detect fault of PRN23, where $P(C)_s$ and $P(C)_c$ respectively represent the $P(C)$ values for the chosen subset and the complete set. Besides $P(C)_s$ is larger than $P(C)_c$. The maximum $P(C)_s - P(C)_c$ is 0.1664 with observation bias of 36m. Therefore, $P(C)$ is increased using the subset fault detection methodology, i.e., $P(C)$ is decreased. In Fig. 10 (b), the $P(\bar{C}D)$ value for subset fault detection methodology is lower than that for complete-set fault detection methodology with observation bias more than about 30m. However, the subset fault detection methodology does not reduce the MDR below its allowable value for all observation bias values. In Fig. 10 (c), the $P(\bar{C}D)$ value for subset fault detection methodology is higher than that for complete-set fault detection methodology with observation bias less than about 50m. Therefore, we observed that the decrease of MDR is at some cost of the FAR addition. The subset fault detection methodology utilized for the large slope faulty satellite is not excellent because its MDR cannot be artificially controlled.

As seen in Fig.11(a), the $P(C)$ value for the chosen subset is higher than that for the complete set. And in Fig.11(b), the $\lg P(\bar{C}D)$ curve for subset fault detection methodology is lower than the $\lg[P(\bar{C}D)]_a$ curve, but not tangent to the $\lg[P(\bar{C}D)]_a$ curve.

Analyzing Fig. 10 and Fig.11, the subset fault detection methodology can reduce MDR. However, it is not an enough reduction for PRN23. The $P(\bar{C}D)$ value is still higher than $P(C\bar{D})_a$ for a certain observation bias interval. Meanwhile, it is an excessive reduction for PRN30 for the $\lg P(\bar{C}D)$ curve is not tangent to the $\lg[P(\bar{C}D)]_a$ curve.

Unlike using threshold amplification fault detection methodology for the small slope faulty satellite, the $\lg[P(\bar{C}D)]$ curve cannot be limited to just tangent to the $\lg[P(\bar{C}D)]_a$ curve using the subset fault detection methodology for the large slope faulty satellite. However, the subset fault detection methodology is really effective on reducing MDR, which is useful to detect a position fault caused by a large slope faulty satellite.

V. A MODIFIED ALGORITHM BASED ON THE CRITICAL SLOPE

Based on the critical slope and two methodologies in the previous sections, we propose a modified LSR algorithm to reduce the fault detection risk of LSR algorithm.

A. SEARCH THE MOST POTENTIALLY FAULTY SATELLITE
The faulty satellite in all-in-view satellites is initially unknown in practical application, thus we cannot decide using which methodology before fault detection. Here we use the correlation analysis between the pseudorange residual vector and the observation error for each visible satellite to search the most potentially faulty satellite.

The correlation analysis was proposed in [28], defining a correlation coefficient, signed as $d_{\omega\varepsilon}^i$, to measure the correlation between the pseudorange residual vector and the observation error of VS_i. The solution of $d_{\omega\varepsilon}^i$ is presented in Appendix B, translated from the original Chinese manuscript.

According to the property of $d_{\omega\varepsilon}^i$, a large $d_{\omega\varepsilon}^i$ means a strong correlation. And the correlation between the pseudorange residual vector and the observation error of the faulty satellite may be the strongest among all-in-view satellite if there was only one faulty satellite. In other words, the satellite with maximum $d_{\omega\varepsilon}^i$ value is most likely to be the faulty satellite. Therefore, VS_i with the maximum $d_{\omega\varepsilon}^i$ value is the most potentially faulty satellite.

B. A MODIFIED LSR ALGORITHM AND ITS PROCESS
The modified LSR algorithm is proposed by comparing the slope of the most potentially faulty satellite with the critical slope. If the slope of the most potentially faulty satellite is larger than the critical slope, the subset fault detection methodology would be used; otherwise the threshold amplification methodology should be used and the amplification factor α would be calculated using the fitted function seen in (44).

The process of the modified LSR algorithm is shown in Fig.12, divided into 3 steps.

step 1: search the most potentially faulty satellite.

step 2: select the fault detection methodology by comparing the slope of the most potentially faulty satellite with the critical slope.

step 3: Detect the position fault via SSE calculation.

Considering the large calculation amount, the numerical solution processes of $Slope_{cri}$ and α are evaded in the modified LSR algorithm. They should be offline completed to ensure that the satellite fault can be real-time detected at a receiver.

Because the $Slope_{cri}$ value and the α-$Slope/Slope_{cri}$ curve are both one to one corresponded to a_v^2 at a fixed all-in-view satellites number, they can be offline numerical solved for each possible value of a_v^2 for different numbers of all-in-view satellites and saved in the receiver.

The numerical solve processes of $Slope_{cri}$ and α for a $Slope/Slope_{cri}$ can be seen in Fig.4 and Fig.6 respectively.
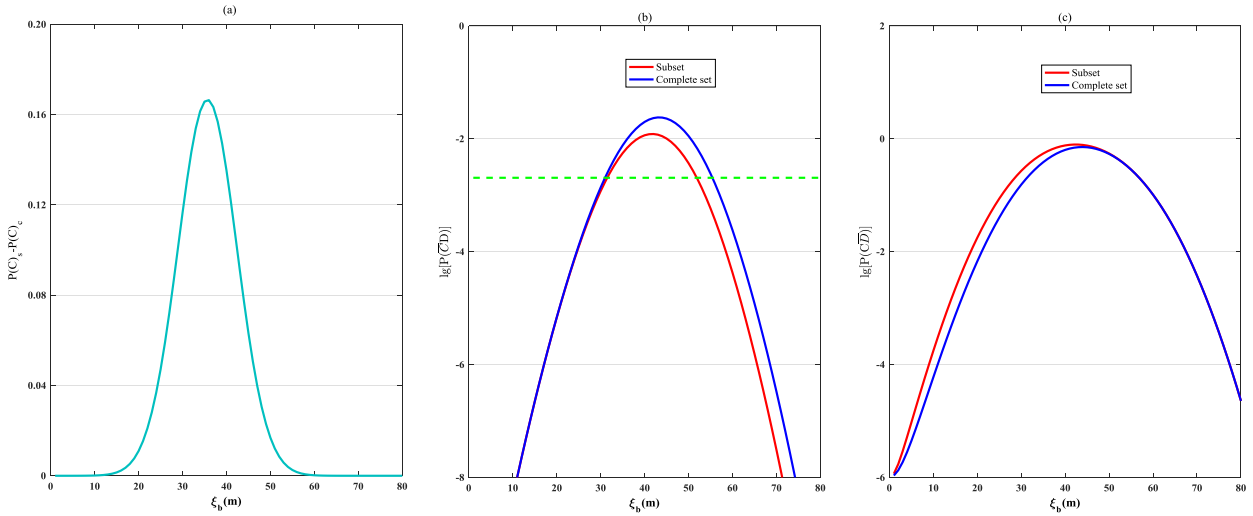
FIGURE 10. Fault detection performance comparison for PRN23 using subset and complete set fault detection methodology. (a) P(C). (b) MDR. (c) FAR.
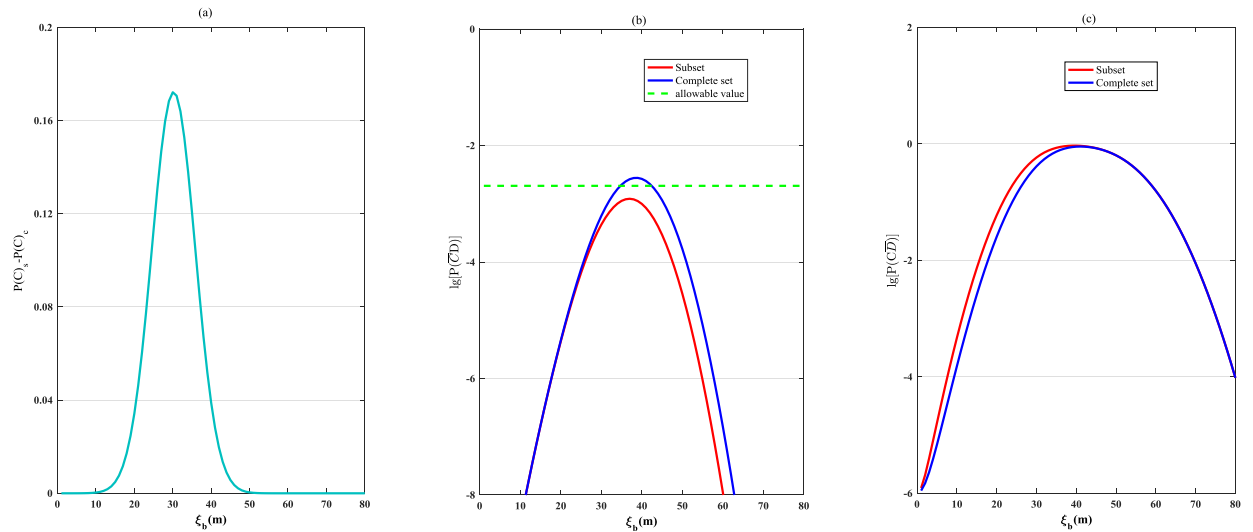

FIGURE 11. Fault detection performance comparison for PRN30 using subset and complete set fault detection methodology. (a) P(C). (b) MDR. (c) FAR.

Because the α-$Slope/Slope_{cri}$ curve can be fitted by the function shown in (44), only the parameters of a and b for the fitted function need to be saved for each a_v^2 value.

C. MATHEMATICAL SIMULATION FOR PERFORMANCE TESTING OF THE MODIFIED LSR ALGORITHM

The performance of modified LSR algorithm might be pulled down by the correlation analysis between the pseudorange residual vector and the observation error, for the most potentially faulty satellite, signed as VS_M, not necessarily being the real faulty satellite, signed as VS_F. For example, if the real faulty satellite owned a large slope and the most potentially faulty satellite owned a small slope, the faulty would more likely to be miss detected because the fault detection threshold is amplified and the identified faulty satellite would not be the real one even if the fault is detected. On the contrary, if the real faulty satellite owned a small slope and the most

potentially faulty satellite owned a large slope, the faulty would more likely to be false alerted because the subset fault detection is used and the identified faulty satellite would not be the real one.

Therefore, a simulation experiment is designed to verify the performance of the modified LSR algorithm on the conditions shown in Tab.1. In this simulation, PRN 2, PRN19, PRN23 and PRN30 are set as the faulty satellite respectively with observation bias from 1 σ_0 to 30 σ_0. 10^6 times of fault detection are implemented for each observation bias value and the observation noise for each visible satellite is the randomly generated WGN with mean 0m and standard deviation 4m at each time. Three kinds of algorithms are used to detect fault, the first two kinds are the LSR algorithm and the modified LSR algorithm. The third kind algorithm is the modified LSR algorithm under the assumption that the most potentially faulty satellite is the
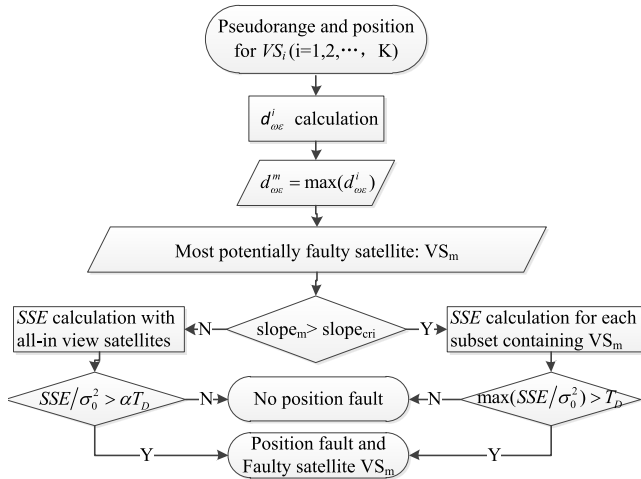
FIGURE 12. A modified LSR algorithm process.

real faulty satellite, abbreviated as the ideal-modified LSR algorithm.

Fig.13 present the probability of that the most potentially faulty satellite and the real faulty satellite are the same, signed as $P(VS_M = VS_F)$, for different observation bias values. $P(VS_M = VS_F)$ for each faulty satellite is different. The curves for the 4 faulty satellites can be sorted as PRN30, PRN19, PRN2 and PRN23 from high to low. Obviously, the faulty satellite with large s_{mm} value owns high $P(VS_M = VS_F)$. And $P(VS_M = VS_F)$ can reach 100% with observation bias larger than 40m,i.e., $20\sigma_0$. Because $P(VS_M = VS_F)$ of PRN 23 is minimum, the performance of modified LSR algorithm for PRN23 is most affected by the correlation analysis among the four satellites, which is analyzed in Fig.14.
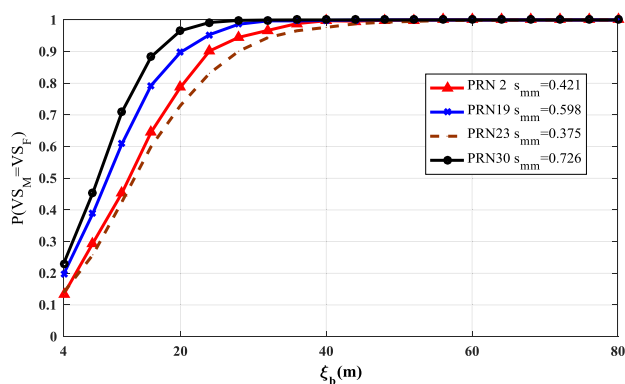

FIGURE 13. $P(VS_M = VS_F)$ for 4 faulty satellites.

Fig.14 (a) presents the $P(C)$ difference between the real and ideal modified LSR algorithms. Obviously, $P(C)$ is decreased because the misjudgment to the real faulty satellite using the correlation analysis. The maximum $P(C)$ difference is about 0.015 with $\xi_b = 9\sigma_0$ (36m). Fig.14 (b) describes the MDR for the three different LSR algorithms. Because of the decrease of $P(C)$, the MDR of the real modified LSR
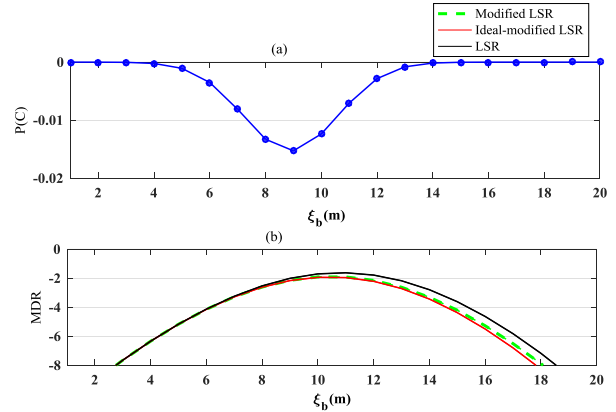

FIGURE 14. Fault detection performance of a modified LSR algorithm for PRN 23.

algorithm is slightly larger than that of the ideal modified LSR algorithm. However, it is still smaller than that of the LSR algorithm. Fig.14 illustrates that the modified LSR algorithm has better fault detection performance than the LSR algorithm even if the misjudgment to the real faulty satellite using the correlation analysis really increases the fault detection risk.

Fig.15 shows the probability of fault detection $P(C)$, and the probability of fault identification $P(VS_f = PRN23|C)$ for PRN23 using the modified LSR algorithm, where VS_f presents the faulty satellite which is finally confirmed. The $P(C)$ of $P(VS_f = PRN23|C)$ curves are almost coincident. The largest difference between $P(C)$ and $P(VS_f = PRN23|C)$ is 1.03×10^{-4} with observation bias of 40m, i.e., 10 σ_0. Therefore, the misjudgment to the real faulty satellite using the correlation analysis slightly decreases the probability of fault identification.
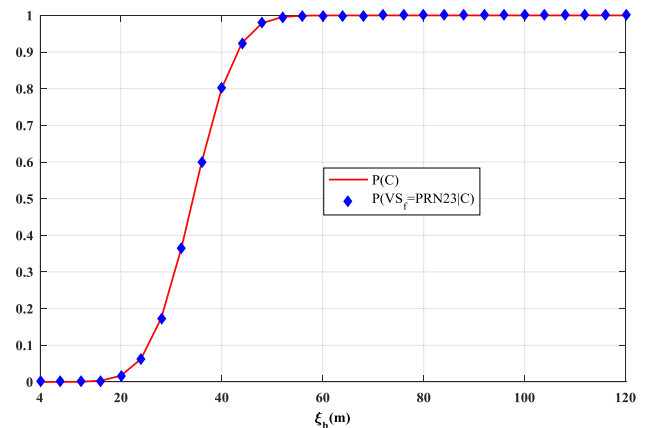

FIGURE 15. Probability comparison for fault detection and fault Identification for PRN23 using the modified LSR algorithm.

D. MATHEMATICAL SIMULATION FOR PERFORMANCE DISPLAYING OF THE MODIFIED LSR ALGORITHM

The performance of the modified LSR algorithm is visually displayed via mathematical simulation, compared with the LSR algorithm. The simulation conditions can be seen in

Tab.6 and the observation noise is randomly generated WGN for each simulation epoch. Under these conditions, $a_v^2 = 1.307$, $[P(\bar{C}D)]_a = 1.825 \times 10^{-3}$, $Slope_{cri} = 1.392$, and the $\alpha - Slope/Slope_{cri}$ fitted function is $\alpha(x) = 1.233 (x^{-1.998} - 1) + 1$.

TABLE 6. Simulation conditions.

Parameter	Value
Constellation	GPS
Masking angle	10°
σ_0	4m
VAL	50m
T_D	38.2583 ($\alpha = 10^{-6}$)
Receiver position	south latitude 30° west longitude 135° height 0 m
Simulation epoch	2018-11-2 10:00:00
Faulty satellite	PRN2/ PRN10
Simulation times	500
Observation bias	0 (1-250 times) and $18\sigma_0$ (251-500 times)

Tab.7 records the slope and α values of each visible satellite. The α value is calculated with the fitted $\alpha - Slope/Slope_{cri}$ function. Comparing with $Slope_{cri} = 1.392$, PRN2 is the only one large slope satellite. And PRN10 owns the minimum slope. Then, we respectively choose PRN2 and PRN10 as the faulty satellite in simulation.

TABLE 7. Slope for each visible satellite.

PRN	2	4	8	9	10
$VSlope_m$	1.860	0.435	0.285	0.325	0.097
α		12.364	29.088	22.320	252.339
PRN	15	17	21	24	26
$VSlope_m$	0.486	0.431	0.617	0.170	0.440
α	9.861	12.598	6.033	82.089	12.079

Fig.16 and Fig.17 respectively show the simulation results setting PRN 2 and PRN 10 as the faulty satellite. The sub-figure(a) presents the *VPE* values and sub-figures(b) and (c) present the values of ratio between the test statistic and its threshold, notated as Ts/T_D.

As seen in Fig.16, the times of VPE exceeding VAL is 35 after injecting 18 σ_0 (72m) observation bias on PRN2, i.e., the probability of VPE exceeding VAL is 14.00%. The miss detection probability of the modified LSR algorithm is 14.4% lower than that of LSR algorithm, 30.0%, for 72 and 105 times of miss detection respectively. Therefore, the MDR for the two LSR algorithms are 0.020 and 0.042 respectively. Although the MDR for the two algorithms exceeds the max allowable value 1.825×10^{-3}, the MDR for modified LSR algorithm is just half of that for LSR algorithm.

As seen in Fig.17 (a), there is no significant change on VPE after injecting 18 σ 0(72m) observation bias on PRN10.
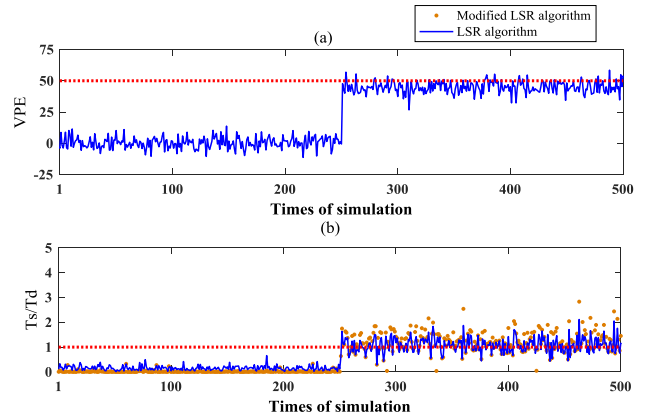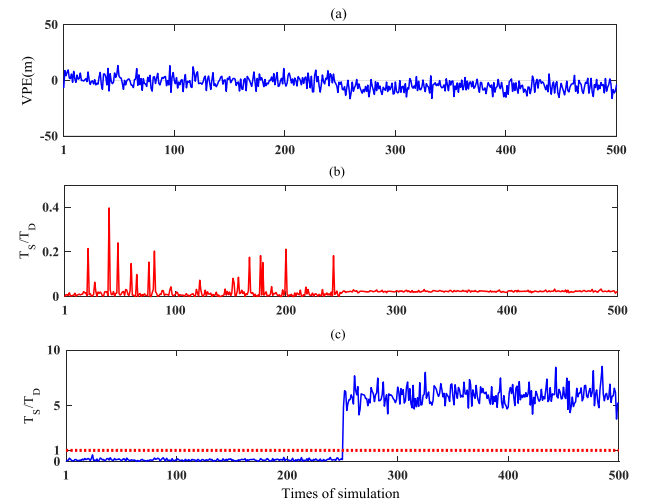

FIGURE 16. VPE and Ts/T_D for PRN2.

FIGURE 17. VPE and Ts/T_D for PRN10.

However, the Ts/T_D value is larger than 5 in 95% confidence and the fault detection probability of LSR algorithm reaches 100% as the seen in Fig.17 (c), which means the position fault will be 100% false alerted with faulty satellite PRN10 owning $18\sigma_0$ observation bias. The Ts/T_D values of modified LSR algorithm after observation bias injection keeps less than 0.1 seen in Fig.17 (b), which means the false alert can be avoided using modified LSR algorithm. The reason for the severely jitter of the Ts/T_D curve during the 0 observation bias period in Fig.17 (b) is that the most potentially faulty satellite judged using correlation analysis is different at each simulation epoch and the T_D is changed according to the correlation analysis result. If PRN2 was judged as the most potentially faulty satellite, the T_D value would not be amplified. And if the other satellites was judged as the most potentially faulty satellite, the T_D value would not be amplified according to its slope value. Therefore, the Ts/T_D curve is significantly jittered during the 0 observation bias period using the modified LSR algorithm.

Fig.16 and Fig.17 visually explains the advantage of the modified LSR algorithm, keeping the trends of *VPE* and Ts/T_D change caused by the observation bias of the faulty satellite consistent. Because the observation bias of a large slope faulty satellite brings large *VPE* change, the Ts/T_D

value is amplified in the modified LSR algorithm. Because the observation bias of a small slope faulty satellite brings small *VPE* change, the Ts/T_D value is diminished in the modified LSR algorithm. In short, the Ts/T_D value of modified LSR algorithm can reflect the *VPE* caused by faulty satellite more accurately than that of LSR algorithm.

VI. CONCLUSION

In this paper, we propose a critical slope for each satellite-user geometry. It is the largest one which satisfies the miss detection risk not exceeding its allowable value in a fixed geometry when using the LSR algorithm to detect faulty satellite. The faulty satellite with slope larger than the critical one will lead to a high MDR, exceeding its allowable value for the observation bias in a certain interval. Whereas the faulty satellite with slope smaller than the critical one will lead to a high FAR, may reaching 100% for the observation bias in a certain interval.

Utilizing the property of the critical slope, a modified LSR algorithm is proposed to reduce the fault detection risk, including the MDR and the FAR. We search the most potentially faulty satellite via correlation analysis between the pseudorange residual vector and the observation error for each visible satellite and then calculate its slope value. Comparing with the critical slope, the subset fault detection methodology would be used when the slope larger than the critical slope while the threshold amplification fault detection methodology would be used when the slope smaller than the critical slope.

The modified algorithm has been used to detect position fault, showing that both the MDR caused by a large slope faulty satellite and the FAR caused by a small slope faulty could be reduced. Especially, the FAR for position fault caused by a small slope faulty satellite is the minimum that makes the MDR not exceeding the allowable value.

APPENDIX

A. DERIVATION OF $a_v = VDOP$

As seen in (4), $A = (H^T H)^{-1} H^T$, thus $AA^T = (H^T H)^{-1}$. Because $a_v^2 = \sum_{i=1}^{K} a_{3i}^2$ is the sum of squares for all elements in Row 3 of A in (4), a_v^2 is the element of Row 3 and Column 3 in matrix AA^T. Therefore, a_v^2 is equal to the element of Row 3 and Column 3 in matrix $(H^T H)^{-1}$, i.e., $a_v = VDOP$.

B. CORRELATION COEFFICIENT BETWEEN THE RESUIDUAL VECTOR AND THE OBSERVATION ERRO

The correlation coefficient between the residual vector and the observation error for VS_i is defined as follows

$$d_{\omega\varepsilon}^i = \frac{\left| \sum_{j=1}^{K} (s_{ij} - \bar{s}_i)(\omega_j - \bar{\omega}) \right|}{\sqrt{\sum_{j=1}^{K} (s_{ij} - \bar{s}_i)^2 \sum_{j=1}^{K} (\omega_j - \bar{\omega})^2}} \tag{45}$$

In (45), $\bar{s}_i = \sum_{j=1}^{K} s_{ij} \bigg/ K$, $\bar{\omega} = \sum_{j=1}^{K} \omega_j \bigg/ K$. ω_j and s_{ij} are shown in (6). $d_{\omega\varepsilon}^i$ has the following properties:

1) $d_{\omega\varepsilon}^i \leq 1$;
2) The larger the value of $d_{\omega\varepsilon}^i$, the stronger the correlation between ε_i and ω, which means the effect from ε_i to ω is more significant;
3) $d_{\omega\varepsilon}^i = 0$ indicates that ε_i and ω are irrelevant, which means that the observation bias for VS_i cannot be detected with ω.

According to the properties of $d_{\omega\varepsilon}^i$, it can be surmised that $d_{\omega\varepsilon}^i$ of the faulty satellite may be the maximum among all of the visible satellites because its observation error can obviously affect the value of ω.

REFERENCES

[1] T. Murphy and M. Harris, "RAIM performance in the post SA era," in *Proc. 21st Int. Tech. Meeting Satell. Division Inst. Navigat. (ION GNSS)*, Savannah, GA, USA, Sep. 2008, pp. 139–150.

[2] H. Leppäkoski, H. Kuusniemi, and J. Takala, "RAIM and complementary Kalman filtering for GNSS reliability enhancement," in *Proc. IEEE/ION Position, Location, Navigat. Symp.*, Apr. 2006, pp. 948–956.

[3] T. Walter and P. K. Enge, "Weighted RAIM for precision approach," in *Proc. ION GPS*, Palm Springs, CA, USA, 1995, pp. 1995–2004.

[4] J. E. Angus, "RAIM with multiple faults," *Navigation*, vol. 53, no. 4, pp. 249–257, 2006.

[5] A. Ene, J. Blanch, and J. D. Powell, "Fault detection and elimination for Galileo-GPS vertical guidance," in *Proc. ION NTM*, San Diego, CA, USA, 2007, pp. 1–11.

[6] Y. C. Lee, "Performance of receiver autonomous integrity monitoring (RAIM) in the presence of simultaneous multiple satellite faults," in *Proc. 60th Annu. Meeting Inst. Navigat. (ION)*, Jun. 2004, pp. 687–697.

[7] B. W. Parkinson and P. Axelrad, "Autonomous GPS integrity monitoring using the pseudorange residual," *Navigation*, vol. 35, no. 2, pp. 255–274, 1988.

[8] J. Blanch, T. Walter, and P. Enge, "RAIM with optimal integrity and continuity allocations under multiple failures," *IEEE Trans. Aerosp. Electron. Syst.*, vol. 46, no. 3, pp. 1235–1247, Jul. 2010.

[9] G. Schroth *et al.*, "Enhancements of the range consensus algorithm (RANCO)," in *Proc. 21st Int. Tech. Meeting Satell. Division Inst. Navigat. (ION GNSS)*, Savannah, GA, USA, 2008, pp. 93–103.

[10] Y. Yang and J. Xu, "GNSS receiver autonomous integrity monitoring (RAIM) algorithm based on robust estimation," *Geodesy Geodyn.*, vol. 7, no. 2, pp. 117–123, 2016.

[11] B. S. Pervan, S. P. Pullen, and J. R. Christie, "A multiple hypothesis approach to satellite navigation integrity," *Navigation*, vol. 45, no. 1, pp. 61–71, 1998.

[12] L.-X. Xu and X.-H. Li, "A receiver clock bias-based GPS RAIM algorithm," *J. Astronaut.*, vol. 32, no. 3, pp. 537–542, 2011.

[13] A. Angrisano, S. Gaglione, and C. Gioia, "RAIM algorithms for aided GNSS in urban scenario," in *Proc. IEEE Ubiquitous Positioning, Indoor Navigat., Location Based Service (UPINLBS)*, Helsinki, Finland, Oct. 2013, pp. 1–9.

[14] L. Wen-Xiang, L. I. Zheng-Rong, and W. Fei-Xue, "A new RAIM method for detecting and correcting weak pseudo-range bias under gradual change," *J. Astronaut.*, vol. 31, no. 4, pp. 1024–1029, 2010.

[15] S. Hai, H. Xinming, L. Wenxiang, X. Bo, and O. Gang, "Research on the RAIM method based on non-coherent accumulation for tiny pseudo-range bias," *J. Astronaut.*, vol. 35, no. 6, pp. 708–712, 2014.

[16] C. Yang, X. Xu, R. Liu, and H. Zhao, "An improved RAIM algorithm based on the total least squares," in *Proc. Int. Conf. Comput. Intell. Secur.*, Dec. 2008, pp. 319–324.

[17] Y. C. Lee, "A position domain relative RAIM method," *IEEE Trans. Aerosp. Electron. Syst.*, vol. 47, no. 1, pp. 85–97, Jan. 2011.

[18] S. Feng, W. Y. Ochieng, D. Walsh, and R. Ioannides, "A measurement domain receiver autonomous integrity monitoring algorithm," *GPS Solutions*, vol. 10, no. 2, pp. 85–96, May 2006.

[19] S. Bhattacharyya and D. Gebre-Egziabher, "Kalman filter–based RAIM for GNSS receivers," *IEEE Trans. Aerosp. Electron. Syst.*, vol. 51, no. 3, pp. 2444–2459, Jul. 2015.

[20] P. Madonna, S. Viola, and L. Sfarzo, "NIORAIM algorithm applied to a multiconstellation GNSS: Analysis of integrity monitoring performances in various phases of flight," in *Proc. IEEE/ION Position, Location Navigat. Symp.*, May 2010, pp. 1258–1263.

[21] Y. C. Lee, "Two new RAIM methods based on the optimally weighted average solution (OWAS) concept," *Navigation*, vol. 54, no. 4, pp. 333–345, 2007.

[22] M. Joerger, S. Stevanovic, S. Langel, and B. Pervan, "Integrity risk minimisation in RAIM part 1: Optimal detector design," *J. Navigat.*, vol. 69, no. 3, pp. 449–467, 2016.

[23] M. Joerger, S. Langel, and B. Pervan, "Integrity risk minimisation in RAIM part 2: Optimal estimator design," *J. Navigat.*, vol. 69, no. 4, pp. 709–728, 2016.

[24] T. Walter, P. Enge, J. Blanch, and B. Pervan, "Worldwide vertical guidance of aircraft based on modernized GPS and new integrity augmentations," *Proc. IEEE*, vol. 96, no. 12, pp. 1918–1935, Dec. 2008.

[25] P. B. Steven, "Navigation integrity for aircraft precision landing using the global positioning system," Ph.D. dissertation, Stanford Univ., Stanford, CA, USA, 1996.

[26] P. Zhang, "Study on positioning performance and receiver autonomous integrity monitoring technology of multi-constellation GNSS," Ph.D. dissertation, School Aerosp. Eng., Beijing Inst. Technol., Beijing, China, 2016.

[27] J. Blanch, T. Walter, and P. Enge, "Satellite navigation for aviation in 2025," *Proc. IEEE*, vol. 100, pp. 1821–1830, May 2012.

[28] S. Chuang and L. Jingnan, "Correspondence based outlier analysis," *J. Wuhan Tech. Univ. Surveying Mapping*, vol. 23, no. 1, pp. 5–9, 1998.

[29] G. H. Golub and C. F. van Loan, "An analysis of the total least squares problem," *SIAM J. Numer. Anal.* vol. 17, no. 6, pp. 883–893, 1980.

[30] S. Hewitson and J. Wang, "GNSS receiver autonomous integrity monitoring (RAIM) performance analysis," *Gps Solutions*, vol. 10, no. 3, pp. 155–170, 2006.

[31] J. A. Blanch, T. Walter, and P. K. Enge, "Critical Positioning for Advanced RAIM," in *Proc. Int. Tech. Meeting Inst. Navigat. (ION)*, Newport Beach, CA, USA, 2012.

[32] J. A. Blanch, T. Walter, and P. K. Enge, "Results on the critical detection statistic for integrity monitoring," in *Proc. Int. Tech. Meeting Inst. Navigat. (ION)*, San Diego, CA, USA, 2013.

[33] M. Joerger, F.-C. Chan, and B. Pervan, "Solution separation versus residual-based RAIM," *Navigation*, vol. 61, no. 4, pp. 273–291, 2014.

DAN SONG received the Ph.D. degree in aerospace science and technology from the Beijing Institute of Technology, in 2018. She is currently pursuing the Ph.D. degree under the guidance of Prof. C. Shi with the School of Electronic and Information Engineering, Beihang University, Beijing, China. Her research interests include the algorithms of INS/GNSS integrated navigation and receiver autonomous integrity monitoring (RAIM).

CHENGDONG XU received the Ph.D. degree from Beihang University, Beijing, China. He is a Professor with the School of Aerospace Engineering, Beijing Institute of Technology, Beijing. His research interests include aircraft design, digital design and manufacturing, satellite navigation, and system simulation.

JING ZHAO received the B.Eng. and M.Eng. degrees from the Taiyuan University of Technology, Taiyuan, China, in 2011 and 2014, respectively, where he is currently pursuing the Ph.D. degree under the guidance of Prof. C. Xu, with the Beijing Institute of Technology. His research interests include GNSS integrity and anti-spoofing.

XUEEN ZHENG received the B.Eng. and M.Eng. degrees from Shengyang Ligong University, Shenyang, China, in 2006 and 2010, respectively. He is currently pursuing the Ph.D. degree under the guidance of Prof. C. Xu with the Beijing Institute of Technology. His research interests include GNSS integrity and ANN.

• • •